

A Rosy e Wolmer

Foreword

Place

Foreword author

Preface

Place, Date

Editors

Acknowledgements

Contents

1	Estimation of optimal inlet boundary conditions for blood flow assessment in abdominal aortic aneurysm using variational data assimilation	1
	S. Paratico, R. Munafò, C. Trenti, P. Dyverfeldt, S. Saitta and E. Votta	
	Glossary	11

List of Contributors

Sara Paratico¹

Riccardo Munafó¹

Chiara Trenti^{2,3}

Petter Dyverfeldt^{2,3}

Simone Saitta⁴

Emiliano Votta¹

¹ Politecnico di Milano, Department of Electronics, Information, and Bioengineering, Milano, Italy

² Division of Cardiovascular Medicine, Department of Health, Medicine and Caring Sciences, Linköping University, Universitetssjukhuset, 581 83 Linköping, Sweden

³ Center for Medical Image Science and Visualization (CMIV), Linköping University, Universitetssjukhuset, 581 83 Linköping, Sweden

⁴ Amsterdam University Medical Center, Department of Biomedical Engineering and Physics, Amsterdam, The Netherlands

Acronyms

AAA	Abdominal aortic aneurysm
BC	Boundary condition
BFGS	Broyden-Fletcher-Goldfarb-Shanno
CFD	Computational fluid dynamics
CMR	Coronary Magnetic Resonance
CN	Crank-Nicolson
FE	Finite Elements
GMRES	Generalized minimal residual method
IPCS	Incremental pressure correction scheme
MRI	Magnetic resonance imaging
NS	Navier Stokes
OSI	Oscillatory shear index
RE	Reynolds number
PDE	Partial differential equation
RMSE	Root Mean Squared Error
TAWSS	Time Averaged WSS
VarDA	Variational data assimilation
WSS	Wall shear stress

Chapter 1

Estimation of optimal inlet boundary conditions for blood flow assessment in abdominal aortic aneurysm using variational data assimilation

S. Paratico, R. Munafò, C. Trenti, P. Dyverfeldt, S. Saitta and E. Votta

Abstract

Blood fluid dynamics impacts vessel wall cells and tissue biomechanics, influencing thrombus formation and vessel wall remodeling. Accurate *in vivo* quantification can thus aid in understanding these mechanisms and patient stratification. Computational fluid dynamics (CFD) and 4D flow MRI are used for this purpose, but both have limitations: CFD involves assumptions and boundary condition simplifications, while 4D flow MRI suffers from low spatial resolution and noise. This study employs variational data assimilation (VarDA) to integrate CFD and 4D flow MRI, yielding a high-resolution, noise-free flow field closely aligned with 4D flow MRI velocity data. To enhance alignment, the optimal inlet velocity profile is determined iteratively via an incremental pressure correction scheme (IPCS). Tested previously on synthetic simple geometries and subsequently on a complex AAA case, this approach demonstrates improved reliability in patient-specific hemodynamic assessment.

Introduction

Alterations in blood fluid dynamics often contribute to the onset or the progress of cardiovascular pathological conditions [Bappoo et al. (2021), Guzzardi et al. (2015), Pozzi et al. (2021)]. Hence, quantifying blood fluid dynamics on a patient-specific basis and non-invasively can support the understanding of pathological mechanisms or the stratification of patients based on the risk for adverse endpoints. To this aim, blood flow field can be reconstructed from clinical imaging, namely 4D flow MRI [Dyverfeldt et al. (2015)], or computed through patient-specific CFD models [Salman and Yalcin (2021)]. However, 4D flow MRI provides indirect and noisy velocity measurements with low spatio-temporal resolution, which often violate mass

S. Paratico e-mail: sara.paratico@mail.polimi.it
Politecnico di Milano

conservation. CFD models offer noiseless, well-resolved velocity fields, but typically require uncertain assumptions on BCs, including inlet velocity BCs. VarDA incorporates *in vivo* velocity data into CFD simulations yielding noiseless, highly resolved velocity fields that respect mass conservation and aligning with observation-based data. The method was tested on a clinical case of AAA, a localized aortic dilation that alters hemodynamics and increase rupture risk [Lattanzi (2020)]. However, VarDA applied to 3D problems in complex geometries proved to be computationally expensive.

Related works

Several studies have explored VarDA in hemodynamics. D’Elia and Veneziani (2013) compared a noise-sensitive splitting method with a control-based approach in 2D Stokes flow simulations. While their method optimized inflow normal stress to match velocity fields, high computational costs limited its application to real 3D scenarios. Later research applied VarDA to the Navier-Stokes (NS) equations, using discrete optimization to incorporate noisy velocity data [D’Elia et al. (2012)]. Tests on a 2D aortic arch and a carotid bifurcation validated VarDA’s ability to reconstruct flow from synthetic data. More advanced applications, including a 3D saccular aneurysm, demonstrated its flexibility in handling Dirichlet and Neumann BCs, adapting the optimization framework for different flow characteristics and constraints. This adaptability enabled integration of gradient-based methods and genetic algorithms to refine boundary controls and improve accuracy [Tiago et al. (2017)]. Koltukluolu and Blanco (2018) showed VarDA’s superiority in maintaining flow congruence near inlets with 4D flow MRI with respect to standard CFD, dynamically adjusting BCs in real time. Funke et al. (2019) application of 4DVarDA to transient blood flow in aneurysms utilized phase contrast-MRI data, highlighting VarDA’s capability to capture complex hemodynamics via iterative boundary input optimization. Additionally, Dokken et al. (2020) multimesh finite element (FE) method enhanced numerical stability and accuracy by allowing flexible BC management across multiple mesh domains with IPCS.

Aim of the work

This study aims to implementing a VarDA method to estimate an optimal inlet BC for a CFD simulation, initially fed by a noisy and uncertain 4D flow MRI-based inlet BC. The method aims to minimizing the mismatch between the CFD solution and velocity data measured *in vivo* by 4D flow MRI, ultimately yielding a highly resolved and noise-free velocity field that is consistent with experimental measurements. We first benchmarked the method on ideal 2D and 3D geometries and then applied it to a patient-specific AAA geometry.

Methods

Data Assimilation Method

The VarDA approach was formulated as an optimization problem constrained by the Navier-Stokes (NS) equations, using the *dolfin-adjoint* library for the adjoint problem. The process follows three steps: running a first numerical simulation with tentative inlet BCs (i.e., the Tape), solving the optimization problem to identify inlet BCs, and running a final numerical simulation yielding the refined velocity and pressure fields (Fig. 1.1).

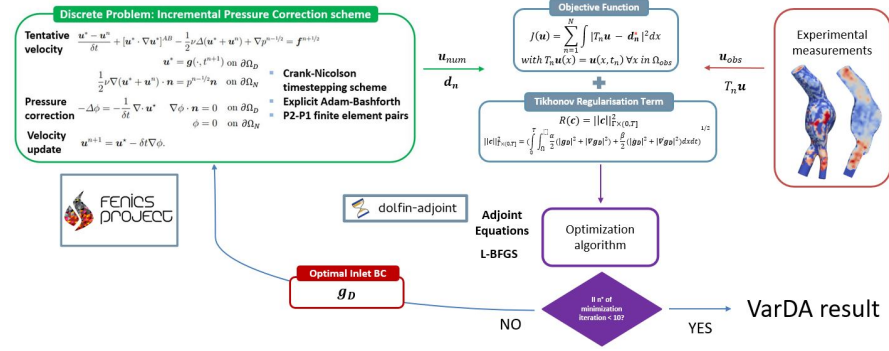


Fig. 1.1: **Top-left:** FE solver solves NS equations with an initial guess for inlet BC; **Top-right:** experimental velocity measurements are taken at discrete points in the domain; **Center:** discrepancy between CFD velocity field and experimental data is minimized by iteratively refining inlet velocity profile with a gradient-based method.

Governing equations of the problem

Blood fluid dynamics follows the NS equations, which express the conservation of linear momentum and mass. Modeling blood as a Newtonian, incompressible fluid [Khalid et al. (2021)], the Eulerian form of the momentum equations reads:

$$\rho_f \left(\frac{\partial \mathbf{u}}{\partial t} + (\mathbf{u} \cdot \nabla) \mathbf{u} \right) - \nabla \cdot \mathbf{T}_f(\mathbf{u}, p) = \rho_f \mathbf{f} \quad \forall x \in \Omega, \quad t > 0 \quad (1.1)$$

where $\mathbf{f} = \mathbf{f}(\mathbf{x}, t)$ represents volumetric forces, ρ_f is blood density (1.06 g/cm^3 [Secomb (2016)]), and $\mathbf{T}_f(\mathbf{u}, p)$ is the Cauchy stress tensor defined as:

$$\mathbf{T}_f(\mathbf{u}, p) = -p\mathbf{I} + \mu(\nabla \mathbf{u} + (\nabla \mathbf{u})^T) \quad (1.2)$$

with blood viscosity μ assumed to be 3.9 cP [Khnouf et al. (2019)]. The conservation of mass for an incompressible fluid is:

$$\nabla \cdot \mathbf{u} = 0 \quad (1.3)$$

Introducing kinematic viscosity $\nu = \frac{\mu}{\rho_f}$, the NS equations become:

$$\partial_t \mathbf{u} + \mathbf{u} \cdot \nabla \mathbf{u} - \nu \Delta \mathbf{u} + \nabla p = \mathbf{f} \quad \text{in } \Omega \times (0, T) \quad (1.4)$$

$$\nabla \cdot \mathbf{u} = 0 \quad \text{in } \Omega \times (0, T) \quad (1.5)$$

The BCs, followed by the initial condition (IC), are:

$$\mathbf{u} = \mathbf{g} \quad \text{on } \partial\Omega_D \times (0, T) \quad (1.6)$$

$$(\nu \nabla \mathbf{u} - p \mathbf{I}) \cdot \mathbf{n} = \mathbf{0} \quad \text{on } \partial\Omega_N \times (0, T) \quad (1.7)$$

$$\mathbf{u} = (0, 0, 0) \quad \text{on } \partial\Omega_s \times (0, T) \quad (1.8)$$

$$\mathbf{u} = \mathbf{u}_0 \quad \text{on } \Omega \times \{0\} \quad (1.9)$$

Equations (1.6)-(1.8) prescribe velocity vectors \mathbf{g} through a function of space and time at the inlet section $\Omega_D \subset \Omega$, zero pressure at the outlet section Ω_N , and no-slip condition on rigid walls of Ω , respectively.

Forward problem definition

The weak and discretized form of NS equations was solved using the FE platform *FEniCS* [Alnæs et al. (2015)]. Through an in house Python script, 2D and 3D fluid domains Ω were discretized into triangular and tetrahedral elements, respectively, with 1-1.5 mm characteristic size and with linear and quadratic shape functions for nodal pressure and velocity, respectively. The explicit Crank-Nicolson (CN) time-integration scheme was applied with a time increment of $\Delta t = 0.001 \text{ s}$. The IPCS proposed in [Dokken et al. (2020)] was implemented. A generalized minimal residual method (GMRES) was chosen as linear solver, with tolerances of 1×10^{-4} for momentum and continuity equations.

Optimization Problem definition

The optimization problem, constrained by NS equations (eq. (1.10)), aimed to minimize a functional $J(u)$ (eq. (1.12)), defined as the difference between the computed and observed velocities.

$$\min_{\mathbf{c}} J(\mathbf{u}) + R(\mathbf{c}) \quad \text{s.t.} \quad F(\mathbf{u}, \mathbf{c}) = 0 \quad (1.10)$$

$$J(\mathbf{u}) = \|\mathbf{u} - \mathbf{u}_{\text{obs}}\|_{L^2(\Omega)} \quad (1.11)$$

To address the ill-posedness of the problem, a Tikhonov regularization term was introduced. It accounts for two terms that are scaled by parameters α and β , where β is set to 0 for steady-state conditions. This reformulation transforms the problem into an unconstrained optimization scenario, more suitable for gradient descent methods.

$$R(\mathbf{c}) = \|\mathbf{c}\|_{L^2(\Omega)}$$

where

$$\|\mathbf{c}\|_{\Gamma \times (0,T]} = \left(\int_0^T \int_{\partial\Omega} \frac{\alpha}{2} \left(|g_D|^2 + |\nabla g_D|^2 \right) + \frac{\beta}{2} \left(|\dot{g}_D|^2 + |(\nabla g)_D|^2 \right) dx dt \right)^{\frac{1}{2}} \quad (1.12)$$

The adjoint approach efficiently computes the total derivative of the functional, yielding the adjoint NS equations that facilitate optimization. The iterative Broyden-Fletcher-Goldfarb-Shanno (BFGS) algorithm, in its L-BFGS variant [Liu and Nocedal (1989)], served as optimizer. Convergence was ensured through Wolfe conditions [Nocedal and Wright (2006)]. The performances of the method were assessed by $J(u)$ value before and after optimization, Root Mean Squared Error (RMSE) between \mathbf{u}_{CFD} and \mathbf{u}_{obs} , and qualitative analysis of the effect on the velocity field through the software *Paraview*.

Benchmark Tests

Preliminary tests - First, preliminary tests were run to compare the computational efficiency of IPCS vs. the coupled scheme on a 2D straight conduit (2DVar) in turbulent and laminar conditions, respectively [Hale et al. (1955)]. The conduit was a longitudinal section of a cylinder with a diameter of 41 mm and a length of 200 mm. Synthetic observations (\mathbf{u}_{obs}) were generated by an auxiliary CFD simulation, prescribing a parabolic velocity profile at the inlet with peak velocity $U_{\text{max}} = 600$ mm/s ($\text{Re} = 6649$) and with $U_{\text{max}} = 50$ mm/s ($\text{Re} = 554$) for turbulent and laminar conditions, respectively. In the Tape, the tentative inlet velocity profile was parabolic with $U_{\text{max}} = 800$ mm/s ($\text{Re} = 8865$) and $U_{\text{max}} = 100$ mm/s ($\text{Re} = 1108$). The iterative minimization of the discrepancy between \mathbf{u}_{CFD} and \mathbf{u}_{obs} was performed to determine the optimal velocity profile for CFD simulations, verifying if it matched the parabolic profile used to generate the synthetic observations.

Progressively demanding tests - Next, the method was benchmarked through three progressively more demanding tests:

1. 2D straight conduit in transient conditions (2DVar+t benchmark) - This benchmark shared the same domain of the 2DVar benchmark. However, both the auxiliary simulation for the generation of the experimental observations and Tape

consisted in a sequence of two transient simulations: in the first simulation, velocity was initially equal to 0 mm/s everywhere in the domain, and at the inlet a parabolic velocity profile was imposed, whose peak velocity increased linearly from 0 to $\frac{U_{\max}}{2}$ over 0.3 s; in the second simulation, the velocity field computed by the first one was used as IC and the inlet velocity parabolic profile was scaled by the time-dependent function $f(t)$:

$$f(t) = \begin{cases} \frac{U_{\max}}{2} \cos\left(\frac{\pi}{T_s}\left(t - \frac{T_s}{2}\right)\right), & \text{if } t \leq T_s \\ \frac{U_{\max}}{2}, & \text{if } T_s < t \leq T_d \end{cases} \quad (1.13)$$

where $T_s = 300$ ms and $T_d = 540$ ms are cardiac cycle's systolic and diastolic phases.

Besides determining the optimal velocity profile for CFD simulations, spatial and temporal regularization terms [eq. (1.13)] were incorporated into the optimization process and subjected to a sensitivity analysis.

2. 3D straight conduit in steady-state conditions (3DVar benchmark) - This benchmark evaluated the computational cost increase when transitioning from a 2D to a 3D problem. The fluid domain was a 3D cylinder with a radius of 30 mm and a length of 200 mm. IC and BCs, as well as the objective function, were identical to those in the 2DVar benchmark.
3. Patient-specific AAA geometry in steady-state conditions (AAA benchmark) - This benchmark aimed to test VarDA in a complex 3D domain using real experimental observations. 4D flow imaging was acquired from an adult male with AAA using a 3T coronary magnetic resonance (CMR) system (Ingenia, Philips Healthcare, Netherlands) at Linkping University Hospital. The 4D flow data were processed with in-house Python code DOI 10.5281/zenodo.7236014 Saitta et al. (2024) and CMR angiography was performed for 3D AAA geometry segmentation. Two tests were carried out with laminar flow in the AAA. In the first test, observations consisted in 4DFlow data acquired during early systole (at the third time frame of the cardiac cycle), while the Tape was generated by a CFD simulation fed by 4DFlow-based inlet velocity profiles. The second test assessed the method's robustness against noise, using an inlet velocity profile, scaled by 0.15, at peak systole to produce the Tape's output. Noisy observations were generated by processing the Tape's output according to Saitta et al. (2024). In addition to already-mentioned metrics, wall shear stresses (WSSs) from final simulation we analyzed using custom Paraview filters.

Results

Computational costs

Numerical experiments were conducted on various setups: a workstation with 24 CPUs and 64 GB RAM for 2DVar and 3DVar and a high-performance computing system with 40 CPUs and 190 GB RAM for 2DVar+t and AAA benchmark. 2DVar took 30 minutes and 3DVar took 6 hours on 12 CPUs; on the other side, 6 hours were required for 2DVar+t and 17 hours for AAA benchmark.

Preliminary tests

In high Reynolds tests, IPCS optimization reduced RMSE from 142.60 mm/s to 6.70 mm/s, while the Coupled scheme faced convergence issues. In low Reynolds conditions, IPCS proved to be five times faster than the Coupled scheme and achieved a final RMSE of 1.76 mm/s compared to 4.22 mm/s for the Coupled scheme.

Progressively Demanding Tests

2DVar + t benchmark - When a zero-velocity field was imposed as IC, the post-optimization velocity field showed inconsistencies with respect to the observations. In particular, a high-velocity region just downstream of the inlet section was obtained, while low velocity values were computed in the rest of the domain. Moreover, these tests did not yield improvements by changing α , and increasing β further worsened the performance. When the initial velocity and pressure fields were set equal to those yielded by the previous post-optimization simulation, the results showed a more homogeneous flow better matching parabolic characteristics and with lower $J+R$ values.

3DVar benchmark - VarDA was performed by varying the magnitude of the spatial regularization term with α set to 10^{-2} , 10^1 , and 10^3 . The lowest value of $J + R$ was achieved with $\alpha = 10^{-2}$, but it did not correspond to the lowest $RMSE$. The velocity field exhibited a peak near the inlet, indicating a loss of continuity. For $\alpha = 10^1$, the lowest $RMSE$ was obtained, and the post-optimization velocity field better reflected the observed data. Increasing α to 10^3 led to significant deviations from the observations, with unexpected velocity behaviors and higher values of $J + R$ and $RMSE$.

AAA benchmark - In first tests, $RMSE$ improved from 59.3 mm/s to 55.1 mm/s, indicating a better alignment with observations. Generating a Tape took about 25 minutes, while optimization required 17 hours with 80 Gb of memory. WSS distribu-

tions from Tape’s output and 3DVar predictions were consistent, identifying regions with high shear stress. WSS distributions from Tape’s output and 3DVar predictions were consistent in terms of location of high WSS regions. Moreover, while enforcing consistency with 4DFlow-based velocity measurements, the 3DVar method yielded a regular and realistic WSS distribution. This is a major difference as compared to the WSS distribution estimated directly from 4DFlow data, which was unrealistic owing to their poor space-resolution and to the impact of noise in the near-wall region.

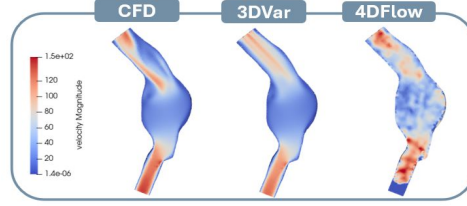


Fig. 1.2: AAA benchmark velocity magnitude maps obtained from Tape (**left**), observations based on 4DFlow MRI (**right**) and assimilated results (**centre**).

In tests with noisy observations, 3DVar effectively reconstructed the velocity field, slightly reducing *RMSE* from 36.8 mm/s to 36.4 mm/s, while maintaining WSS predictions consistent with CFD results, particularly at the iliac bifurcation.

Discussion

From 2DVar+t to 3DVar

The 2DVar+t reveals challenges due to inertial effects and short simulation durations, causing reconstruction defects from incomplete flow development. Extending simulation time for optimization is impractical due to high computational costs. A potential solution includes proper initialization of CFD simulations and implementing a checkpointing method to reduce computational costs by using only the last cardiac cycle for gradient calculations. Moreover, a key difference between 2DVar+t and 3DVar is the flow field’s response to regularization. In 2DVar+t, increasing α has minimal effect due to dominant time-dependent effects, reducing spatial regularization’s impact. Additionally, increasing β deteriorates the results, a challenge not present in 3DVar, emphasizing the difficulty of balancing temporal and spatial regularization in dynamic flows. Conversely, in 3DVar, moderate α values (10^1) significantly improve the velocity field, reducing inlet peaks and lowering *RMSE*. However, excessive regularization ($\alpha = 10^3$) causes unrealistic velocity patterns.

AAA benchmark

AAA benchmark effectively reconstructs the velocity field in AAA geometry, maintaining high consistency with the data obtained from 4D flow imaging. It identifies high shear stress regions despite challenges due to lower resolution of 4D flow data near boundaries. The method remains robust against noise, indicating real-world applicability.

Conclusions

This project advances cardiovascular hemodynamic analysis by validating the VarDA method, demonstrating IPCS's superiority in computational efficiency and accuracy. While challenges in transient flow analyses remain, ongoing research will further enhance VarDA's application in cardiovascular medicine.

References

- Alnæs MS, Blechta J, Hake JE, Johansson A, Kehlet B, Logg A, Richardson C, Ring J, Rognes ME, Wells GN (2015) The fenics project version 1.5. *Archive of Numerical Software* 3, doi:10.11588/ANS.2015.100.20553
- Bappoo N, Syed MB, Khinsoe G, Kelsey LJ, Forsythe RO, Powell JT, Hoskins PR, McBride OM, Norman PE, Jansen S, Newby DE, Doyle BJ (2021) Low shear stress at baseline predicts expansion and aneurysm-related events in patients with abdominal aortic aneurysm. *Circulation: Cardiovascular Imaging* 14(12):e013160, doi:10.1161/CIRCIMAGING.121.013160, URL <https://www.scopus.com/inward/record.uri?eid=2-s2.0-85122903899&doi=10.1161%2fCIRCIMAGING.121.013160&partnerID=40&md5=030cc3d35d356dae7a8ac11b414f44a7>, cited by: 15; All Open Access, Bronze Open Access
- D'Elia M, Veneziani A (2013) Uncertainty quantification for data assimilation in a steady incompressible navier-stokes problem. *ESAIM: Mathematical Modelling and Numerical Analysis* 47:1037–1057, doi:10.1051/m2an/2012056
- D'Elia M, Perego M, Veneziani A (2012) A variational data assimilation procedure for the incompressible navier-stokes equations in hemodynamics. *Journal of Scientific Computing* 52:340–359, doi:10.1007/s10915-011-9547-6
- Dokken JS, Johansson A, Massing A, Funke SW (2020) A multimesh finite element method for the navierstokes equations based on projection methods. *Computer Methods in Applied Mechanics and Engineering* 368, doi:10.1016/j.cma.2020.113129
- Dyverfeldt P, Bissell M, Barker AJ, Bolger AF, Carlhll CJ, Ebbers T, Francios CJ, Frydrychowicz A, Geiger J, Giese D, Hope MD, Kilner PJ, Kozerke S, Myerson S, Neubauer S, Wieben O, Markl M (2015) 4d flow cardiovascular magnetic resonance consensus statement. *Journal of Cardiovascular Magnetic Resonance* 17, doi:10.1186/s12968-015-0174-5
- Funke SW, Nordaas M, yvind Evju, Alns MS, Mardal KA (2019) Variational data assimilation for transient blood flow simulations: Cerebral aneurysms as an illustrative example. *International Journal for Numerical Methods in Biomedical Engineering* 35, doi:10.1002/cnm.3152

- Guzzardi DG, Barker AJ, Van Ooij P, Malaisrie SC, Puthumana JJ, Belke DD, Mewhort HE, Svystonyuk DA, Kang S, Verma S, Collins J, Carr J, Bonow RO, Markl M, Thomas JD, McCarthy PM, Fedak PW (2015) Valve-related hemodynamics mediate human bicuspid aortopathy: Insights from wall shear stress mapping. *Journal of the American College of Cardiology* 66(8):892–900, doi:10.1016/j.jacc.2015.06.1310, URL <https://www.scopus.com/inward/record.uri?eid=2-s2.0-84939485996&doi=10.1016%2Fj.jacc.2015.06.1310&partnerID=40&md5=fb7993e7f5ab08ace4ac409a69d309d5>, cited by: 356; All Open Access, Bronze Open Access
- Hale J, McDonald D, Womersley J (1955) Velocity profiles of oscillating arterial flow, with some calculations of viscous drag and the Reynolds number. *The Journal of Physiology* 128(3):629–640, doi:10.1113/jphysiol.1955.sp005330
- Khalid AK, Othman ZS, Shafee CTM (2021) A review of mathematical modelling of blood flow in human circulatory system. IOP Publishing Ltd, vol 1988, doi:10.1088/1742-6596/1988/1/012010
- Khounf R, Karasneh D, Abdulhay E, Abdelhay A, Sheng W, Fan ZH (2019) Microfluidics-based device for the measurement of blood viscosity and its modeling based on shear rate, temperature, and heparin concentration. *Biomedical Microdevices* 21, doi:10.1007/s10544-019-0426-5
- Koltukluolu TS, Blanco PJ (2018) Boundary control in computational haemodynamics. *Journal of Fluid Mechanics* 847:329–364, doi:10.1017/jfm.2018.329
- Lattanzi S (2020) Abdominal aortic aneurysms: pathophysiology and clinical issues. doi:10.1111/joim.13060
- Liu DC, Nocedal J (1989) On the limited-memory bfgs method for large scale optimization. doi:10.1007/BF01589116
- Nocedal J, Wright SJ (2006) *Numerical Optimization*, 2nd edn. Springer, doi:<https://doi.org/10.1007/978-0-387-40065-5>
- Pozzi S, Domanin M, Forzenigo L, Votta E, Zunino P, Redaelli A, Vergara C (2021) A surrogate model for plaque modeling in carotids based on robin conditions calibrated by cine mri data. *International Journal for Numerical Methods in Biomedical Engineering* 37(5), doi:10.1002/cnm.3447, URL <https://www.scopus.com/inward/record.uri?eid=2-s2.0-85101747829&doi=10.1002%2fcnm.3447&partnerID=40&md5=9354f6a788248f5999e385072c274c73>, cited by: 8
- Saitta S, Carioni M, Mukherjee S, Schönlieb CB, Redaelli A (2024) Implicit neural representations for unsupervised super-resolution and denoising of 4d flow mri. *Computer Methods and Programs in Biomedicine* 246:108057, doi:10.1016/J.CMPB.2024.108057
- Salman HE, Yalcin HC (2021) Computational modeling of blood flow hemodynamics for biomechanical investigation of cardiac development and disease. doi:10.3390/JCDD8020014
- Secomb TW (2016) Hemodynamics. *Comprehensive Physiology* 6:975–1003, doi:10.1002/cphy.c150038
- Tiago J, Guerra T, Sequeira A (2017) A velocity tracking approach for the data assimilation problem in blood flow simulations. *International Journal for Numerical Methods in Biomedical Engineering* 33, doi:10.1002/cnm.2856

Glossary

Abdominal aortic aneurysm Localized dilation of the abdominal aorta, which can lead to rupture and severe complications if untreated.

Boundary condition Condition that defines the values of variables in a physical system at the boundaries of a spatial domain to solve partial differential equations.

Broyden-Fletcher-Goldfarb-Shanno Numerical optimization algorithm used to solve unconstrained minimization problems.

Computational fluid dynamics Field that uses numerical methods to analyze and solve problems involving fluid flows.

Coronary Magnetic Resonance Medical imaging technique based on magnetic resonance to visualize coronary blood flow and heart tissue.

Crank-Nicolson Implicit numerical method used to solve parabolic and hyperbolic partial differential equations, often employed in CFD simulations.

Generalized minimal residual method Iterative method for solving non-symmetric linear systems, widely used in CFD and other scientific computing fields.

Incremental pressure correction scheme Numerical scheme for solving Navier-Stokes equations that separates velocity and pressure calculations into multiple steps.

Magnetic resonance imaging Non-invasive medical imaging technique that uses magnetic fields and radio waves to produce detailed images of tissues inside the body.

Navier-Stokes System of equations describing the motion of viscous fluids, fundamental in many fluid dynamics applications.

Oscillatory shear index Measure of the directional oscillation of shear stress on the walls of a blood vessel, often associated with vascular disease susceptibility.

Partial differential equation Equation involving partial derivatives of a function with respect to multiple variables, commonly used to model physical phenomena.

Root Mean Squared Error Statistical measure of the difference between predicted and observed values, used to evaluate the accuracy of a model.

Time Averaged Wall Shear Stress Time-averaged value of shear stress on vessel walls, relevant for studying hemodynamics.

Variational data assimilation Method that combines mathematical models and observational data to improve estimates of physical states, commonly used in fluid dynamics and meteorology.

Wall shear stress Stress exerted by a fluid on the wall of a vessel or conduit, crucial for analyzing hemodynamics and vascular diseases.